# A 3D Hepatocyte Model with Composite Nanofibers that Reproduced Human *in vivo* Drug Clearance Profiles

Rudolph Park[1] and Chengpeng Chen[1,*]

1. Department of Chemistry and Biochemistry, University of Maryland Baltimore County

*Corresponding to:
Dr. Chengpeng Chen
Department of Chemistry and Biochemistry
University of Maryland Baltimore County
Baltimore, MD, USA, 21250
cpchen@umbc.edu +14104553053

## Abstract

This study presents a novel *in vitro* 3D hepatocyte model that contains a nanofibrous scaffold designed to mimic the extracellular matrix (ECM) of the human liver, both structurally and biochemically. A modular 3D-printed device housing the ECM scaffold was also developed, readily fitting in well plates. HepaRG hepatocytes cultured on the scaffold exhibited enhanced metabolic activity compared to traditional 2D cultures, indicating improved hepatocyte functionality. Drug clearance studies with lidocaine, clozapine, and fluoxetine demonstrated significantly faster clearance rates on the scaffold, closely aligning with *in vivo* results from literature, while 2D cultures showed limited metabolic capacity. This model offers a physiologically relevant platform for hepatocyte studies. The findings underscore the model's potential to advance preclinical drug development by replicating liver-specific functions *in vitro*.

## Introduction

It costs 1-2.5 billion US dollars and takes 10-15 years for a new drug to be fully developed[1-3]. Drug development is divided into preclinical and clinical stages. Preclinical studies focus on understanding the mechanisms and targets of candidate drug compounds and validating efficacy and possible toxicity. Drug candidates that pass preclinical screening are routed into clinical trials with human subjects. However, with current technologies, compounds that pass preclinical testing and validation have a low probability (<10%) of being launched as a drug[4]. This high failure rate, largely caused by the limited predictive power of preclinical models, not only drives up the cost and time for drug development, which will eventually be propagated as patients' burdens, but can also lead to unexpected tragic outcomes in clinical trials or even after a drug is marketed. A recent example is the compound BIA10-2474, which killed and disabled human subjects after comprehensive preclinical assessments[5].

Currently, preclinical studies rely heavily on cell culture and animal models[6]. Cell culture in well-established containers such as flasks, Petri dishes, and well plates is simple, scalable, relatively cost-efficient, and yields fast results. Nonetheless, growing cells in a 2D monolayer on a flat surface does not provide *in vivo* cell-cell and cell-extracellular matrix (ECM) interactions, and thus may not represent human physiology. The ECM is a network of micro-/nano-fibers composed of glycoproteins, collagen, fibronectin, elastin, and other macromolecules[7, 8]. Emerging evidence suggests that in addition to acting as a nesting niche for cells, the chemical and physical properties of the ECM (e.g., stiffness, microstructures[9]) are key regulators of intracellular biochemical processes[10-14]. On the other hand, although animal models provide 3D tissue structures, drug responses from animals can differ drastically from humans[15, 16]. While lab animals and humans have only slight differences in their genomes, these differences can be significantly amplified during transcriptional and post-transcriptional processes, causing major phenotypic variances[17], such as in hepatocyte enzyme activity[18, 19].

Therefore, new preclinical models that align more closely to human *in vivo* responses are being actively studied. Hitherto, two technologies have mainly been investigated: 3D-cell culture-based physiological models[20] and organs-on-a-chip models[21, 22]. By incorporating ECM materials such as hydrogels[23] and/or fibrous scaffolds

in human cell culture, 3D-cell culture-based physiological models enhance intercellular and cell-ECM interactions, making cell functions and activities more closely match *in vivo* behaviors[24]. For instance, 3D spheroid tumor models exhibit more complex, *in vivo*-like responses to therapeutics vs. flat, 2D cultures[25]. Organs-on-a-chip can connect different cell types[26] in physiologically relevant architectures[27] with finely tuned flows to nourish cells, remove waste, and provide physical stimuli (e.g., shear stress[10]) to replicate relevant microenvironments. Such systems can be used to study interactions between organs, such as between the gut and liver, which are known to impact drug toxicity[28].

Investigating absorption, distribution, metabolism, elimination, and toxicity (ADMET) is an essential part of drug development[2, 29]. Drug metabolism is mainly carried out by the liver *in vivo*[30]. Understanding the metabolism of a drug candidate is critical: 1) certain drugs must be metabolized by the liver before they can be excreted, and knowing the metabolism rates is indispensable to assess drug and metabolite accumulation issues[29, 31]; 2) prodrugs need to be metabolized to become active compounds[32, 33]; 3) orally delivered drugs are extensively metabolized in the liver before reaching circulation, and understanding the metabolism rates guides predictions of bioavailability[34]; 4) the metabolism rates determine the dosage regimes of a drug[35].

Integrating reliable and predictive liver models in the drug development pipeline will reduce cost burdens and safety issues. Indeed, various enlightening models have recently been investigated. For instance, Ewart et al.[36] reported a liver-on-a-chip model on a polydimethylsiloxane (PDMS) microfluidic apparatus, containing sinusoidal endothelial cells, stellate cells, and primary human hepatocytes sandwiched in Matrigel ECMs. The model showed toxicity responses to clozapine and olanzapine. A similar model has also been tested to show cross-species toxicity responses from primary hepatocytes to bosentan[37]. However, while toxicity responses are an important component of preclinical testing, hepatocyte models that can reproduce physiological drug metabolism/clearance profiles are limited in literature. Although a few models using primary cells are reported[38], stringent statistical comparisons with *in vivo* data are not available.

Hence, we report our effort to develop a 3D hepatocyte model based on a composite nanofibrous scaffold that mimics both the microstructures of the native liver

ECM and its biochemical composition. Instead of using primary human hepatocytes, which have limited availability and are difficult to trace (e.g., donor health/medical history), or hepatocyte-like cells derived from pluripotent stem cells, which are expensive and challenging to maintain[39], we used HepaRG hepatocytes in our model[40, 41]. HepaRG is an immortalized cell line that can be differentiated into human hepatocyte cells in one simple step[42]. Numerous pieces of evidence have demonstrated the cells preserve liver-specific genes, protein expression, and functions[40, 42-44]. We found that HepaRG progenitor cells were successfully seeded and differentiated on the scaffold and exhibited typical hepatic functions. More importantly, by treating the differentiated hepatocytes with well-documented drugs that need to be metabolized before excretion, we discovered that hepatocytes on our model reproduced *in vivo* drug clearance rates, while cells in conventional well plates (2D culture) showed significantly slower drug clearance and reduced clearing capacities. Also, to make the model more translational—after all, end users tend to implement the simplest models, we developed modular 3D-printed holders and batch-produced scaffold inserts, which can be assembled in seconds and housed in standard well plates. The ease of use of the fibrous scaffold and its ability to modulate *in vivo*-like functions of HepaRG hepatocytes represents a novel and significant improvement in preclinical modeling.

## Experimental

### Decellularized ECM Extraction

Fresh porcine liver tissues were obtained from local slaughterhouses, cut into ~1 $cm^3$ cubes, and put in a 2 L Erlenmeyer flask. The cubes were rinsed with doubly deionized (DDI) water then soaked in 1.5 L decellularization solution composed of 0.5% Triton X-100 (A16046.AP, Thermo Fisher, Pittsburgh, PA, USA) and 47.6 mM ammonium hydroxide (AX1303-3, MilliporeSigma, St. Louis, MO, USA) and placed on a stir plate in 4 °C, stirring at 180 rpm. The decellularization solution was changed every 24 hours for 7 days. The decellularized ECM (dECM) was then thoroughly rinsed with DDI water, patted dry with paper towels, placed in two 250 mL weigh boats (10803-170, VWR International, Radnor, PA, USA), and frozen at -80 °C, after which it was lyophilized and ground into a coarse powder. A total of 300-400 mg of coarsely powdered dECM was

digested with 40 mL of 3500 U/mL pepsin (P7000, MilliporeSigma, St. Louis, MO, USA) in 0.01 M HCl solution for 24 hours at 37 °C on an orbital shaker, 60 rpm. The solution was neutralized with 0.1 M NaOH to pH 8.0 to permanently denature the pepsin. The digested dECM solution was centrifuged for 20 min at 10,000 x g, 4 °C in a high-speed centrifuge (Avanti J-E, Beckman Coulter, Brea, CA, USA), the supernatant collected in 50 mL conical tubes, lyophilized for 72 hours and stored in -20 °C.

dECM Insert Preparation

The dECM electrospinning solution was made by combining two solutions: Solution 1 consisted of 20% w/v polycaprolactone (PCL) with an average molecular weight 80,000 (440744, MilliporeSigma, St. Louis, MO, USA) in 2,2,2-trifluoroethanol (TFE) (A10788, Thermo Fisher, Pittsburgh, PA, USA). Solution 2 consisted of 20% w/v pepsinated dECM powder in TFE + 5% acetic acid (AC42322, Fisher Scientific, Pittsburgh, PA, USA). 1.5 mL of Solution 2 was pipetted into 1.5mL of Solution 1 to produce 3.0 mL of the dECM electrospinning solution (10% w/v PCL in TFE, 10% w/v dECM in TFE + 2.5% acetic acid). Electrospinning was performed on the TL-Pro-BM electrospinning machine (Tong Li, Shenzhen, China). As shown in **Figure S1A** in the Supplementary Information (SI), a 50 mm wide metal mandrel was covered by a polystyrene (PS) sheet with 14.5 mm diameter circular holes cut with a Hobby 5S laser cutter (Full Spectrum Laser, Las Vegas, NV, USA). The circular holes defined the nanofiber deposition locations. A 5 mL Leur-Lok syringe (30964, BD, MA, USA) was used to pump the electrospinning solution through a 24 G metal blunt needle placed 17 cm from the surface of the mandrel. The syringe pump was set to a flow rate of 0.25 mL/hr. The mandrel was rotated at 300 rpm, and the voltage of the mandrel was set to -5 kV, while the needle was set to +17 kV. The electrospinning was conducted for 4 hours. The needle scanned back and forth across the width of the mandrel at a rate of 5 mm/s to deposit a uniform layer of nanofibers (**Figure S1B**). After the electrospinning was completed, the PS sheet was placed in the laser cutter to cut out circular inserts of 18.5 mm diameter (**Figure S1C** and **Figure S1D**). The laser-cutting process also heat-fused the edges of the nanofiber and PS layers.

Scanning Electron Microscope (SEM) Imaging of the Scaffolds

An SEM (FEI Nova NanoSEM 450, Thermo Fisher, Pittsburgh, PA, USA) was used to image the dECM inserts at high (2,000x - 20,000x) magnification. An insert was mounted on a pin stub SEM mount (75210, Electron Microscopy Sciences, Hatfield, PA, USA), sputter coated with gold, and imaged on the SEM. The DiameterJ[45] plugin for ImageJ/FIJI was used to measure the diameters of the fibers in SEM images.

Picrosirius Red (PSR) Staining

The Picrosirius Red Stain Kit (24901, Polysciences, Warrington, PA, USA) was used to stain collagen in the scaffold inserts. The insert was rinsed with DDI water then soaked in 0.5 mL of Solution B (Picrosirius Red F3BA stain) for 60 minutes. The insert was then rinsed with Solution C (0.1 N HCl) for 1 minute, twice, followed by rinsing in DDI water and then in 70% ethanol for 60 s. The stained inserts were then imaged or placed in a plate reader (SpectraMax i3x, Molecular Devices, San Jose, CA, USA) with the well-scanning mode to detect PSR fluorescence signals (560 nm excitation, 650 nm emission).

Collagen I Antibody Labelling

The CoraLite Plus 488-conjugated Collage Type I Monoclonal antibody (CL488-67288, Proteintech, Rosemont, IL, USA) was used to label the dECM inserts to visualize collagen from the extracted ECM in the nanofibers. The inserts were rinsed 3x with PBS, fixed for 10 min in 4% paraformaldehyde solution, rinsed 3x in wash buffer (PBS + 0.1% Tween 20) for 5 min, and gently rocked in blocking solution (PBS + 0.1% Tween 20 + 1% bovine serum albumin (0332-25G, VWR International, Radnor, PA, USA)) for 60 min at room temperature. The blocking solution was then replaced with 1 mL of antibody solution (1:200 dilution of antibody in blocking solution). The insert was rocked gently overnight at 4 °C, covered with foil to protect it from light. The insert was then washed 3x in wash buffer for 5 min and placed on a WillCo glass bottom dish (HBSB-5040, WillCo Wells, Amsterdam, The Netherlands) with 20 µL SlowFade Diamond Antifade Mountant (S36972, Thermo Fisher, Pittsburgh, PA, USA).

Confocal Microscopy

A confocal laser scanning microscope (LSM 900, Zeiss, Oberkochen, Germany) was used to image the fluorescence from PSR-stained and collagen I antibody-labeled inserts. A 561 nm laser was used to excite the PSR-stained sample with a detection band

of 613-700 nm. A 488 nm laser was used to excite the CoraLite 488 fluorophore conjugated to the Collagen I antibody with a detection band of 505-550 nm. A 63x objective (oil immersion) was used for both the PSR and CoraLite 488 imaging.

3D-printed Insert Holder Assembly

The dECM insert holder assembly was composed of an insert holder (**Figure 2A**, **Figure 2C**) and a hollow lid (**Figure 2A**, **Figure 2B**) that were screwed together, with a silicone O-ring (19 mm OD, 16 mm ID) (**Figure 2A**, **Figure 2D, Figure 2E**) to create a tight seal. The insert holder and hollow lid were 3D printed (Form 3B, Formlabs, Somerville, MA, USA) using the biocompatible BioMed Clear Resin (RS-C2-BMCL-01, Formlabs, Somerville, MA, USA). Prior to seeding cells, the 3D-printed parts and O-rings were sterilized by autoclaving. The scaffold inserts were sterilized inside a biological safety cabinet (BSC) by soaking in 70% ethanol and placed in the insert holder to dry under UV light. After drying, an O-ring was placed on the insert and compressed by screwing the hollow lid into the insert holder. The assembly was then placed in a 12-well plate (10861556, VWR International, Radnor, PA, USA) (**Figure 2E**, lid removed for clarity). See **Figure S2** and **Figure S3** for detailed information on the designs and dimensions of the 3D-printed insert holder and hollow lid.

HepaRG Culture and Differentiation

Undifferentiated HepaRG cells (HPR101, Biopredic International, Saint-Gregoire, France) were thawed and maintained in the growth medium composed of HepaRG growth medium supplement with antibiotics (ADD710C, Biopredic International) in Williams E medium with GlutaMAX supplement (32551020, Thermo Fisher, Pittsburgh, PA, USA). The growth medium was refreshed every 2-3 days over 7 days of proliferation in a T75 flask. The flask was then rinsed twice with 5 mL PBS prior to adding 5 mL of 37 °C trypsin (25200056, Thermo Fisher, Pittsburgh, PA, USA) and incubated at 37 °C for 10 min. Growth media (5 mL) was added to the flask to neutralize the trypsin, and the contents of the flask were transferred to a 15 mL conical tube and centrifuged for 5 min @ 2,000 rpm (SCL456, Southwest Science, Trenton, NJ, USA). The supernatant was decanted, and the cell pellet was resuspended in 5-7 mL of growth medium by gentle pipetting. The cells were counted using the EVE automated cell counter (NanoEntek, Seoul, South Korea), and the cell suspension was diluted to 500,000 cells / mL. For the flat culture condition,

the cell suspension was pipetted into four wells of a 12-well plate (1 mL into each well). For the 3D insert culture condition, the cell suspension was pipetted into four dECM insert holder assemblies in the same 12-well plate (1 mL into each assembly).

The growth medium for the flat and dECM inserts was refreshed 6-18 hours after seeding, and then every 2-3 days over 7 days of proliferation. To start differentiation, the growth medium was replaced with 1 mL of 50% growth medium and 50% differentiation medium composed of HepaRG differentiation medium supplement with antibiotics (ADD711C, Biopredic International, Saint-Gregoire, France) in Williams E medium with GlutaMAX supplement (32551020, Thermo Fisher, Pittsburgh, PA, USA). Afterward, the medium was replaced with 1 mL differentiation medium every 2-3 days.

Urea Measurement

Urea in phenol red-free cell differentiation medium was quantified using a colorimetric Urea Assay Kit III (MAK471, MilliporeSigma, St. Louis, MO, USA). Phenol red-free differentiation medium was composed of HepaRG differentiation medium supplement with antibiotics (ADD711C, Biopredic International) in phenol red-free Williams E medium (A1217601, Thermo Fisher, Pittsburgh, PA, USA) and GlutaMAX 100X supplement (35050061, Thermo Fisher, Pittsburgh, PA, USA) diluted to 1X final concentration. An aliquot of 0.75 mL of 24-hr culture medium was collected for urea quantification following the assay kit's manual.

Albumin Assay

The Human Albumin ELISA Kit (ab179887, Abcam, Cambridge, UK) was used to quantify albumin in the cell culture media according to vendor protocols. A 1:400 dilution of the 24-hour culture sample was used for the ELISA assay.

MTS Assay

The MTS Assay Kit (ab197010, Abcam, Cambridge, UK) was used to measure the metabolic activity of differentiated HepaRG cells 13-43 days after differentiation. For each well of flat or dECM insert culture, the differentiation medium was replaced with 500 µL of phenol red-free differentiation medium + 50 µL MTS Reagent Solution. A blank with 20 µL MTS Reagent Solution added to 200 µL of phenol red-free differentiation medium was also prepared. The cell culture and blank were incubated at 37 °C for 2 hours, rocking at 20 rpm,10° tilt (02217765, Fisher Scientific, Pittsburgh, PA, USA). 220 µL of the cell

culture and blank were pipetted into a 96-well plate, and the absorbance was measured on a plate reader (SpectraMax i3x, Molecular Devices, San Jose, CA, USA) at 490 nm.

Drug Metabolism Analysis

A 1 µM solution of lidocaine (L7757, MilliporeSigma, St. Louis, MO, USA) was prepared using a stock solution of 20 mM lidocaine in DMSO (042780.AK, Thermo Scientific, Pittsburgh, PA, USA) that was filter sterilized. The flat and dECM inserts with the HepaRG cells were cultured in 0.75 mL of 1 µM lidocaine in the differentiation medium for 24 hours with 50 µL samples of media taken at 0, 2, 4, 8, and 24 hours. The 12-well plate containing the flat and dECM insert cell cultures was rotated on an orbital shaker (KJ-201BD, Kang Jian Medical, Taizhou City, China) at 30 rpm in a humid 37 °C incubator, 5% $CO_2$. A 400 nM solution of clozapine (C2460000, MilliporeSigma, St. Louis, MO, USA) was prepared using a stock solution of 30.6 mM clozapine in DMSO (042780.AK, Thermo Scientific, Pittsburgh, PA, USA) that was filter sterilized. The flat and dECM inserts with the HepaRG cells were cultured in 1 mL of 400 nM clozapine in the differentiation medium for 24 hours with 50 µL samples of media taken at 0, 2, 4, 8, and 24 hours. The 12-well plate containing the flat and dECM insert cell cultures was rocked at 20 rpm, 10° tilt (02217765, Fisher Scientific, Hampton, NH, USA) in a humid 37 °C incubator, 5% $CO_2$. A 400 nM solution of fluoxetine (F07501G, Fisher Scientific, Hampton, NH, USA) was prepared using a stock solution of 10 mM fluoxetine in DMSO (042780.AK, Thermo Scientific, Pittsburgh, PA, USA) that was filter sterilized. The flat and dECM inserts with the HepaRG cells were cultured in 1 mL of 400 nM of fluoxetine in the differentiation medium for 72 hours with 50 µL of supernatant taken at 0, 4, 8, 24, 48, and 72 hours. The 12-well plate containing the flat and dECM insert cell cultures was rocked at 20 rpm, 10° tilt on a rocking shaker (02217765, Fisher Scientific, Hampton, NH, USA) in a humid 37 °C incubator, 5% $CO_2$.

Standards of each drug were prepared, and 50 µL of each standard was collected at the same time as the 0-hour sample. Each 50 µL sample and standard was pipetted into a 1.5 mL microtube and diluted with 0.45 mL LC/MS Grade Methanol (A456-1, Fischer Scientific, Hampton, NH, USA). The samples were stored at -80 °C for 2 hr to precipitate proteins, the microtubes were then centrifuged (5415 D, Eppendorf, Hamburg, Germany) for 15 min @ 13,200 rpm in 4 °C and 0.35 mL of the supernatant was pipetted into a 2

mL screw thread Autosampler vial (033919, Fisher Scientific, Hampton, NH, USA) and capped with an autosampler vial cap (13622182, Fisher Scientific, Hampton, NH, USA). The vials were loaded onto the autosampler rack of a triple quadrupole LC-MS/MS (LCMS-8045, Shimadzu Corporation, Kyoto, Japan) for drug analysis. Using multiple reaction monitoring (MRM) in positive mode, the following precursor and product m/z ratios were used based on analyzing the standards: lidocaine (235.1 and 86.1), clozapine (327.1 and 269.75) and fluoxetine (310.1 and 43.95). The sample injection volume was 3 µL for all three drugs, and a Luna Omega 1.6 µm Polar C18 column with an inner diameter of 50 × 2.1 mm (00B-47480AN, Phenomenex, Torrance, CA, USA) was used for all three drugs. Mobile phase A was LC/MS grade water with 0.6% formic acid, and mobile phase B was LC/MS grade methanol with 0.6% formic acid. The pump profiles for each drug are shown in **Figure S4**. For each drug, a standard curve was calculated and used to quantify the concentration of the media samples taken at various time points.

*In vivo* data estimation from the literature

*In vivo* clearance curves of lidocaine and clozapine were taken from the following literature of *in vivo* studies: lidocaine[46-52], clozapine[53-59]. Figures for drug concentration in blood (serum or plasma) vs. time in these publications were reanalyzed to obtain the human *in vivo* data.

For the intrinsic clearance data, the following literature was analyzed: lidocaine[60-62], clozapine[63-66]. For reports with the unit per kg, the numbers were multiplied by 70 kg, the average weight of a healthy adult. To normalize the *in vivo* intrinsic clearance data in the aforementioned literature to per cell, the published results that 1 g human liver tissue contains $116x10^6$ hepatocytes[67] and an adult human liver weighs 1561g on average[68] were used.

Cell Counting

Cells cultured on flat surfaces and on dECM inserts were rinsed in PBS, lysed in 0.3 mL RIPA buffer (J52624, Thermo Fisher, Pittsburgh, PA, USA) diluted to 1X, and collected into microtubes followed by 90 sec of sonication (2 sec on, 4 sec off) using an ultrasonic homogenizer (Pulse 150, Benchmark Scientific, South Plainfield, NJ, USA). The lysed cell solution was then centrifuged for 12 min at 13,200 rpm at 4 °C (5415 D, Eppendorf, Hamburgh, Germany). An aliquot of 10 µL of the supernatant was used in a

Bradford assay (23246, Thermo Fisher, Pittsburgh, PA, USA) to quantify the cell number (OD=595 nm). A calibration curve between known cell numbers (EVE, NanoEntek, Seoul, South Korea) and the Bradford assay signals was prepared to elucidate cell numbers in the lysed samples.

Calculations and Statistics

Intrinsic clearance rates (CL) were calculated from experimental data (remaining concentrations as a function of time) with the following equations[69]. The volume of media in the experiments, which was 750 µL for lidocaine and 1000 µL for clozapine, was used for V. The CL was then normalized to per cell based on the cell counting protocol above.

$$C=C_0 \cdot e^{-kt} \qquad \text{Equation 1}$$

*C is apparent concentration of a drug, $C_0$ is the initial concentration, t is time in hr*

$$CL=k \cdot V \qquad \text{Equation 2}$$

*CL is clearance, k is constant from Equation 1, V is distribution volume*

For statistical analyses, the replicate numbers and error bar information were detailed in figure captions. Most error bars were standard deviation (SD). All statistical analysis and figures were generated using GraphPad Prism (GraphPad Software, Boston, MA, USA). Student t-tests and ANOVA were applied for significance analyses. The p values were noted between data groups in the figures wherever necessary. A significant difference was determined only when a p-value was less than 0.05.

## Results and Discussion

The scaffold and setup

We aimed to create a scaffold biologically relevant to the liver ECM in terms of microstructures and biochemical composition. Literature suggests that the native liver ECM is a fibrous network, with estimated ECM fiber diameters ranging from 100 to 500 nm[70-72]. Thus, we used electrospinning to generate nanofibers similar in thickness to those in the native ECM. Electrospinning transforms a polymer solution into nano-/micro-fibers by pumping the solution through a syringe needle at a high voltage, forming a Taylor cone[73]. By varying parameters such as voltage, needle diameter, flow rate, and distance to the collecting platform, the fiber size, orientation, porosity, and layer thickness can be tuned[74]. Polycaprolactone (PCL), a biocompatible polymer, was used as the base material to make the fibers[75, 76]. Meanwhile, cut pieces of porcine liver, which have proven to be similar to the human liver for various biological applications[77, 78], were decellularized to collect the native decellularized ECM (dECM), which was then ground, digested by pepsin and lyophilized. This dECM was added to the PCL solution before electrospinning so that the fibers would contain the native ECM components. Ideally, a larger ratio of the native dECM to PCL would be more biorelevant. However, we observed that if the native dECM exceeded the amount of PCL (weight), the dECM started to precipitate and form layers while in the electrospinning solution. Therefore, we made the solution with 10% PCL (w/v) and 10% (w/v) dECM, which remained homogenous for electrospinning.

**Figure 1A** is a Scanning Electron Microscopic (SEM) view of the composite (PCL + dECM) fibers, and **Figure 1B** shows the fiber diameter distribution. As shown in **Figure S1** in the Supplementary Information, fibers were deposited onto a polystyrene (PS) sheet with precut holes. After electrospinning, the sheet with fibers was laser-cut again around the outside of each hole to generate circular inserts. What remained was a PS ring with a layer of nanofibers on top, fused by the heat generated from the laser cutting. A total of 38 dECM inserts could be prepared in one electrospinning session, which enhanced efficiency and enabled experiments to be conducted on inserts from the same batch, reducing possible variations. **Figure 1C** compares two inserts: PCL-only fibers (left) and PCL + dECM fibers (right). The inserts were incubated with Picrosirius red, a common dye in histology to stain collagen[79]. After thorough rinsing, the dECM insert remained red,

compared to the PCL-only fibers which were white. Because Picrosirius red is moderately fluorescent[80], we scanned the inserts with a plate reader and observed fluorescent signal heatmaps on the fibers with dECM (bottom panel of **Figure 1C**). Further, **Figure 1D** shows fluorescent microscopic views of the composite (PCL + dECM) fibers stained with Picrosirius red, and **Figure 1E** shows staining by collagen I antibodies conjugated with CoraLite 488 of the composite fibers. Moreover, Fourier Transform Infrared (FTIR) spectroscopy was conducted over the fiber layers. As shown in **Figure 1F**, plain PCL fibers showed clusters of peaks between 1000-1200 $cm^{-1}$ and 1400-1500 $cm^{-1}$, mainly corresponding to -C-O stretching and -C-H bending in PCL. However, with the inclusion of the dECM in the electrospinning solution, the resulting fibers showed a broad FTIR peak above 3000 $cm^{-1}$ (arrow), a typical signal of -OH groups. New peaks at 1540 $cm^{-1}$ and 1640 $cm^{-1}$ strongly indicate secondary amide (peptide bonds; inset of **Figure 1F**). These FTIR peaks suggested the presence of proteins and thus further confirmed the successful inclusion of the native dECM in the fibers.

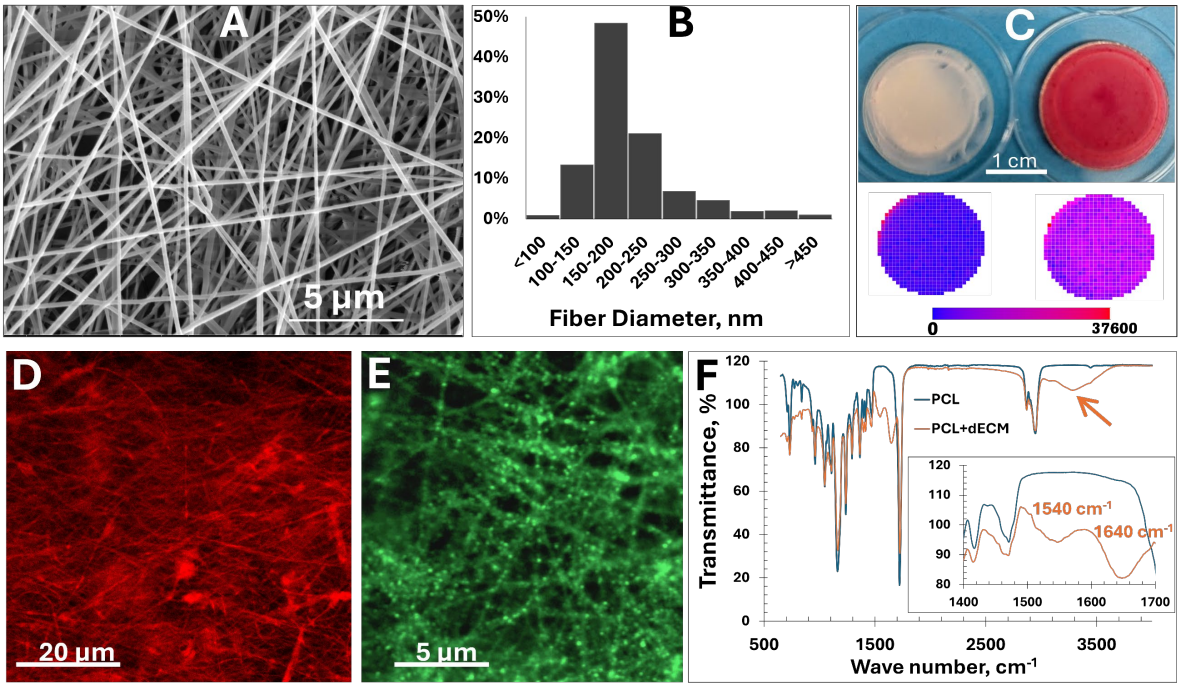


**Figure 1**. (**A**) An SEM view of the composite (PCL+dECM) nanofibrous scaffold. (**B**) Histogram of the fiber diameter distribution (percentage). (**C**) Picrosirius red staining of PCL (left) and PCL+dECM (right) scaffolds after thorough rinsing. Fluorescence of the scaffolds was scanned by a plate reader (bottom) at 560 nm excitation and 650 nm emission, the scale bar shows fluorescent intensity from 0 (blue) to 37600 (red) units. (**D**) Fluorescence microscopy view of Picrosirius red-stained PCL+dECM fibers. (**E**) Fluorescence microscopy view of PCL+dECM fibers stained by anti-porcine-collagen I antibody conjugated CoraLite 488. (**F**) FTIR spectra of PCL (blue) and PCL+dECM (orange) fibers. The inset shows the spectra with a zoomed-in view between 1400 and 1700 $cm^{-1}$.

An insert holder was created to help seed cells onto the dECM insert and house them in a 12-well plate, as detailed in **Figure S1. Figure 2A** demonstrates the assembly of the dECM insert into the 3D-printed insert holder device, with the bottom insert holder and a top hollow lid. After a circular insert was placed in the holder, a silicone O-ring was placed onto the insert before the hollow lid was screwed into the insert holder via the printed threads. **Figures 2B and 2C** show the CAD design views of the lid and holder, respectively, and **Figure 2D** shows an assembled device. **Figures S2** and **S3** in the SI show detailed engineering sketches with the dimensions of the parts. The entire assembly fits in a standard 12-well plate (**Figure 2E**), demonstrating it can easily be integrated into the cell culture workflow of most laboratories. The 3D-printed parts and O-rings can be

reused after rinsing and autoclaving to reduce plastic waste and cost. In the discussion below, hepatocytes cultured on the composite (PCL+dECM) nanofibrous scaffold are denoted as "on dECM," and cells cultured 2D in a regular 12-well plate well are "on flat".

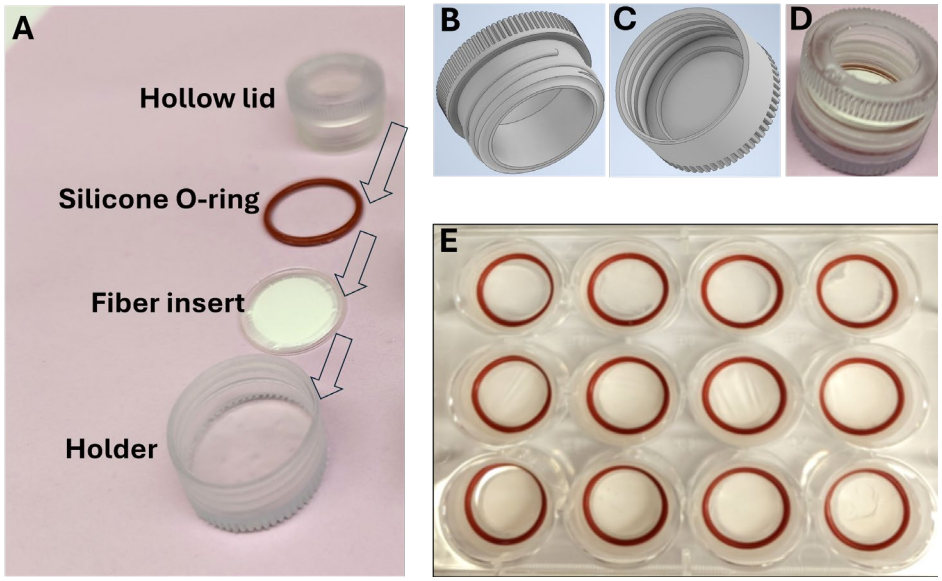


**Figure 2**. (**A**) 3D-printed holder device to house a fiber insert. (**B, C**) The CAD designs of the hollow lid and holder, respectively. (**D**) A picture of an assembled setup. (**E**) The insert holders fit in a standard well-plate for easy integration into cell-culture workflows. The hollow lids were not included to show the inserts and O-rings.

Fundamental characterization of the cells

We evaluated HepaRG cells after 13-14 days of differentiation on the fibrous dECM inserts. As shown in **Figure 3A**, although the number of cells on dECM appeared to be less than on flat, the difference was not significant. There were over 200,000 cells for both conditions. **Figure 3B** shows confocal microscopic views (top and sides) of hepatocytes in the scaffold. Clearly, the cells could infiltrate by ~50 μm into the fibrous layer to form a 3D culture. Hepatocytes were characterized by the ability to synthesize albumin and produce urea, two key fundamental functions of the cells[81]. As suggested by **Figures 3C** and **3D**, cells on both culture substrates showed albumin and urea production, indicating successful differentiation of HepaRG progenitors to hepatocytes. Interestingly, we did not observe significant differences in albumin production from cells on flat vs. on dECM, suggesting that some biosynthesis pathways of HepaRG hepatocytes might not be affected by the ECM. In contrast, cells on dECM produced significantly more urea than on flat, indicating that the metabolic activities of the hepatocytes might be enhanced by the ECM. Further experiments aligned with this observation, where the metabolic activity as measured by the MTS assay (**Figure 3E**) was significantly higher from cells on dECM than on flat for up to 43 days. Between Day 13 and Day 20, cells on both substrates showed increased MTS metabolism (although not significant for cells on flat), and thus, cells within this time frame were used for the following studies.

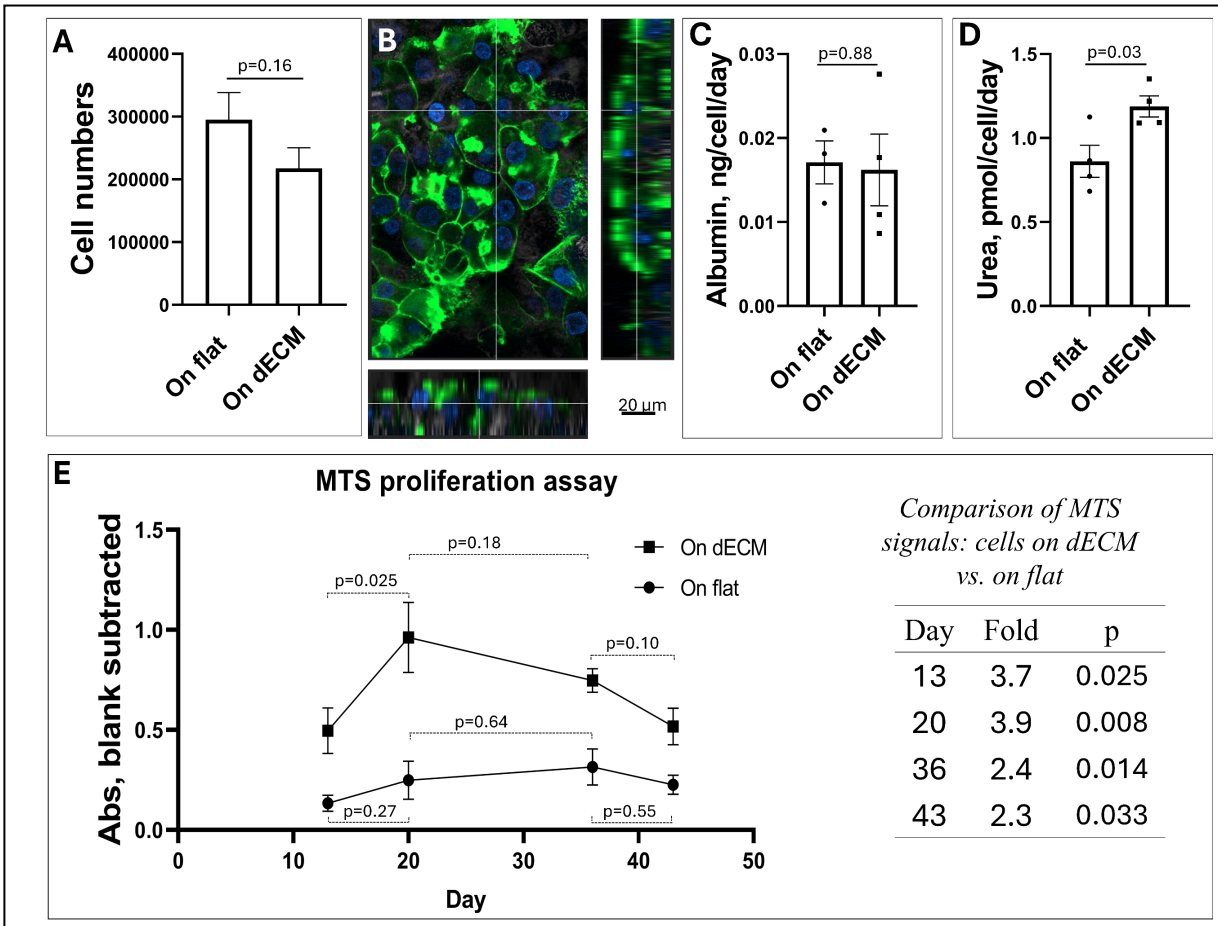


*Comparison of MTS signals: cells on dECM vs. on flat*

| Day | Fold | p |
|---|---|---|
| 13 | 3.7 | 0.025 |
| 20 | 3.9 | 0.008 |
| 36 | 2.4 | 0.014 |
| 43 | 2.3 | 0.033 |

**Figure 3**. Hepatocytes in a regular well-plate were denoted as "on flat", and hepatocytes on our 3D scaffold made of PCL+dECM were denoted as "on dECM". (**A**) Cell numbers under the two culture conditions. N>20 for both, error bar=SD. (**B**) Confocal microscopy view of hepatocytes on dECM. The cells could infiltrate via the pores between fibers by ~50 µm. (**C, D**) Quantified albumin and urea production from hepatocytes. N=3 for on flat and 4 for on dECM, error bar=SD. (**E**) The MTS assay results and analyses. N=4 for both, error bar=SD.

Drug clearance investigations

To explore the scaffold's possible role in enhancing drug metabolism/clearance by the HepaRG hepatocytes, we chose drugs that 1) need to be metabolized by the liver before excretion, with limited direct excretion, 2) are well-studied and well-documented with abundant *in vivo* data available in the literature. The first drug tested was lidocaine[82], a common anesthetic, which is mainly metabolized by CYP3A4 to monoethylglycinexylidide (MEGX), with less than 10% direct excretion[83] (**Figure 4A**). **Figure 4B** depicts the concentration of lidocaine in the media of hepatocytes cultured on flat and on dECM as a function of time. The cells on dECM continued to clear the drug for 24 hours, while those on flat stopped after only 2 hours. By comparing the time needed to reduce the concentration to 50% of the peak level, the hepatocytes on dECM did not show a significant difference from *in vivo*, but cells on flat were significantly slower (**Figure 4C**). Finer comparisons at different time intervals (**Figure 4D**) further validated that the hepatocytes on flat were significantly slower in lidocaine clearance than *in vivo* and cells on dECM. After 24 hours, hepatocytes on dECM cleared ~80% of lidocaine, comparable to *in vivo* results, but cells on flat could only clear ~14%. Intrinsic clearance was also calculated (**Figure 4E**), with the *in vivo* clearance averaging 0.30 nL/hr/cell. Our model with HepaRG hepatocytes on dECM had 0.37 nL/hr/cell, and the conventional well plate model (on flat) cleared lidocaine at only 0.10 nL/hr/cell. Statistical analyses revealed no significant difference between HepaRG hepatocytes on dECM and *in vivo*, but the clearance by cells on flat was significantly lower.

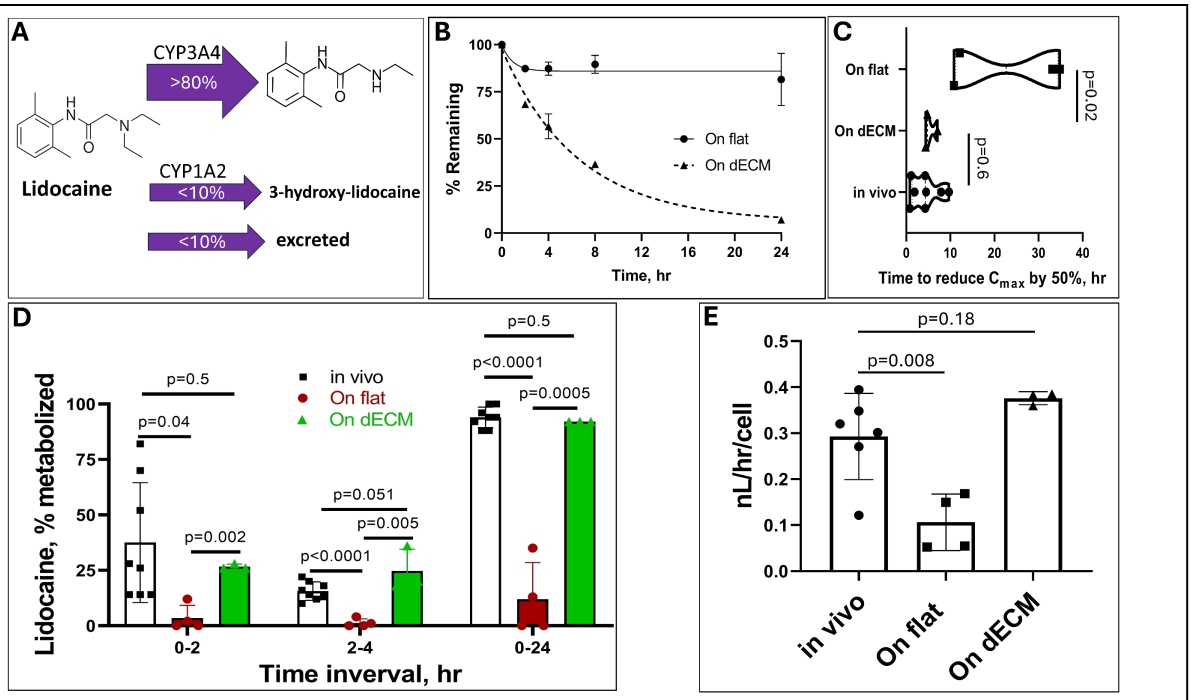


**Figure 4**. Hepatocytes in a regular well-plate were denoted as "on flat", and hepatocytes on our 3D scaffold made of PCL+dECM were denoted as "on dECM". (**A**) Major lidocaine pathways. (**B**) Lidocaine clearance by hepatocytes on flat vs. on dECM. N=3 for both, error bar=SD. (**C**) Comparisons of the time needed to remove 50% of lidocaine. N=3 for on flat and on dECM. (**D**) Finer comparison of percentage lidocaine being removed at different temporal intervals. N=4 for on flat and 3 for on dECM. Error bar=SD. (**E**) Comparison of intrinsic clearance rate of lidocaine by hepatocytes on flat and on dECM vs. *in vivo* data from literature. N=4 for on flat and 3 for on dECM. Error bar=SD.

The next drug we investigated was clozapine[84], an antipsychotic medication, which needs to be fully metabolized before excretion (**Figure 5A**). Clozapine is primarily metabolized by CYP1A2 and CYP3A4 to norclozapine. As with lidocaine, we observed faster clearance of the drug by the hepatocytes on dECM than on flat (**Figure 5B**). The error bars for the flat controls were large because we found the cells started to die with the clozapine, but not the cells on dECM, even with the same drug concentrations. As shown in **Figure 5C**, the time needed to reduce the highest concentration of clozapine to half was not significantly different between cells on dECM and *in vivo* data, while the time was statistically and dramatically longer for cells on flat. Comparisons with finer time intervals (**Figure 5D**) showed the same trends and alignments. Analyses of intrinsic clearance (**Figure 5E**) also confirmed that our dECM model was physiologically relevant, with the flat well-plate model significantly less capable.

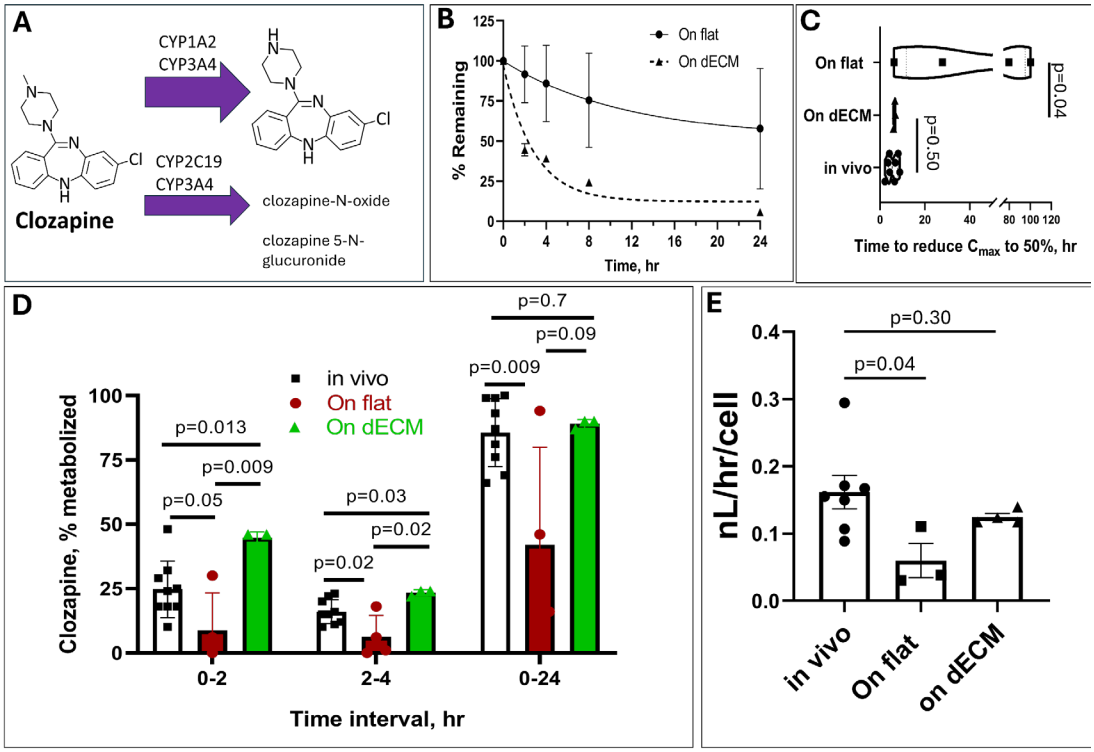


**Figure 5**. Hepatocytes in a regular well-plate were denoted as "on flat", and hepatocytes on our 3D scaffold made of PCL+dECM were denoted as "on dECM". (**A**) Major clozapine pathways. (**B**) Clozapine clearance by hepatocytes on flat vs. on dECM. N=3 for both, error bar=SD. (**C**) Comparisons of the time needed to remove 50% of Clozapine. N=3. (**D**) Finer comparison of percentage clozapine being removed at different temporal intervals. N=4 for on flat and 3 for on dECM. Error bar=SD. (**E**) Comparison of intrinsic clearance rate of clozapine by hepatocytes on flat and on dECM vs. *in vivo* data from literature. N=4 for on flat and 3 for on dECM.Error bar=SD.

The third drug investigated was fluoxetine[85], a selective serotonin reuptake inhibitor commonly used to treat depression. As shown in **Figure 6A**, over 95% of fluoxetine needs to be metabolized before excretion[86]. After measuring the fluoxetine in the media over 72 hours, we observed the results shown in **Figure 6B**. Although hepatocytes cultured on dECM cleared more fluoxetine in the first four hours than cells on flat, the clearance stopped for both thereafter. The stopped clearance was likely caused by metabolites of fluoxetine, such as S-norfluoxetine, which can inhibit CYP2D6[85], the key enzyme for fluoxetine metabolism (**Figure 6C**). These data highlight the necessity of including permeable excretion models to couple with liver models in future studies for efficient removal of metabolites, as occurs *in vivo*, for certain drug clearance studies.

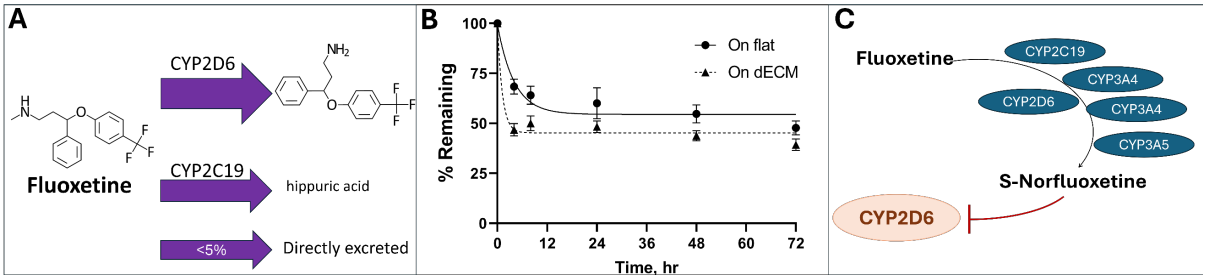


**Figure 6**. Hepatocytes in a regular well-plate were denoted as "on flat", and hepatocytes on our 3D scaffold made of PCL+dECM were denoted as "on dECM". (**A**) Major fluoxetine pathways. (**B**) Fluoxetine clearance by hepatocytes on flat vs. on dECM. N=3 for both. Error bar=SD. (**C**) Fluoxetine metabolite, S-norfluoxetine, inhibits CYP2D6 in turn, the major enzyme metabolizing fluoxetine.

## Conclusion

We demonstrated that a composite nanofibrous scaffold composed of PCL and native porcine liver ECM components enabled enhanced metabolic activities of HepaRG hepatocytes compared to conventional 2D cultures. Combined with a modular 3D-printed holder device fitting in a standard 12-well plate, this hepatic model can easily be integrated into existing cell culture workflows. With this 3D cell culture model, we tested well-documented drugs with *in vivo* data and found that the 3D model significantly enhanced drug clearance vs. the 2D well-plate model. More importantly, the drug clearance times and rates on our model were comparable with published *in vivo* data without significant differences. This 3D model thus holds promises to facilitate hepatocyte studies during preclinical drug development, especially given that it reproduced the *in vivo* observations with a widely accessible cell source (HepaRG), rather than primary human hepatocytes or stem cells.

## REFERENCES


(1) DiMasi, J. A.; Grabowski, H. G.; Hansen, R. W. Innovation in the pharmaceutical industry: New estimates of R&D costs. *J Health Econ* **2016**, *47*, 20-33. DOI: 10.1016/j.jhealeco.2016.01.012

(2) Singh, N.; Vayer, P.; Tanwar, S.; Poyet, J.-L.; Tsaioun, K.; Villoutreix, B. O. Drug discovery and development: introduction to the general public and patient groups. *Frontiers in Drug Discovery* **2023**, *3*. DOI: 10.3389/fddsv.2023.1201419

(3) Congressional Budget Office. *Research and Development in the Pharmaceutical Industry* **April 2021**, *www.cbo.gov/publications/57025*.

(4) Dowden, H.; Munro, J. Trends in clinical success rates and therapeutic focus. *Nat Rev Drug Discov* **2019**, *18* (7), 495-496. DOI: 10.1038/d41573-019-00074-z

(5) Kaur, R.; Sidhu, P.; Singh, S. What failed BIA 10-2474 Phase I clinical trial? Global speculations and recommendations for future Phase I trials. *J Pharmacol Pharmacother* **2016**, *7* (3), 120-126. DOI: 10.4103/0976-500X.189661

(6) Allio, T. The FDA Animal Rule and its role in protecting human safety. *Expert Opin Drug Saf* **2018**, *17* (10), 971-973. DOI: 10.1080/14740338.2018.1518429

(7) Karamanos, N. K.; Theocharis, A. D.; Piperigkou, Z.; Manou, D.; Passi, A.; Skandalis, S. S.; Vynios, D. H.; Orian-Rousseau, V.; Ricard-Blum, S.; Schmelzer, C. E. H.; et al. A guide to the composition and functions of the extracellular matrix. *FEBS J* **2021**, *288* (24), 6850-6912. DOI: 10.1111/febs.15776

(8) Hussey, G. S.; Dziki, J. L.; Badylak, S. F. Extracellular matrix-based materials for regenerative medicine. *Nature Reviews Materials* **2018**, *3* (7), 159-173. DOI: 10.1038/s41578-018-0023-x

(9) Saraswathibhatla, A.; Indana, D.; Chaudhuri, O. Cell-extracellular matrix mechanotransduction in 3D. *Nat Rev Mol Cell Biol* **2023**, *24* (7), 495-516. DOI: 10.1038/s41580-023-00583-1

(10) Jones, C. G.; Huang, T.; Chung, J. H.; Chen, C. 3D-Printed, Modular, and Parallelized Microfluidic System with Customizable Scaffold Integration to Investigate the Roles of Basement Membrane Topography on Endothelial Cells. *ACS Biomaterials Science & Engineering* **2021**, *7* (4), 1600-1607. DOI: 10.1021/acsbiomaterials.0c01752 (acccessed 2023-08-03 00:50:04).

(11) Huang, T.; Jones, C. G.; Chung, J. H.; Chen, C. Microfibrous Extracellular Matrix Changes the Liver Hepatocyte Energy Metabolism via Integrins. *ACS Biomater Sci Eng* **2020**, *6* (10), 5849-5856. DOI: 10.1021/acsbiomaterials.0c01311

(12) Huang, T.; Terrell, J. A.; Chung, J. H.; Chen, C. Electrospun Microfibers Modulate Intracellular Amino Acids in Liver Cells via Integrin β1. *Bioengineering* **2021**, *8* (7), 88. DOI: 10.3390/bioengineering8070088 (acccessed 2023-08-03 00:47:19).

(13) Dutta, R. C.; Dutta, A. K. Cell-interactive 3D-scaffold; advances and applications. *Biotechnol Adv* **2009**, *27* (4), 334-339. DOI: 10.1016/j.biotechadv.2009.02.002

(14) Dityatev, A.; Schachner, M.; Sonderegger, P. The dual role of the extracellular matrix in synaptic plasticity and homeostasis. *Nat Rev Neurosci* **2010**, *11* (11), 735-746. DOI: 10.1038/nrn2898

(15) Attarwala, H. TGN1412: From Discovery to Disaster. *J Young Pharm* **2010**, *2* (3), 332-336. DOI: 10.4103/0975-1483.66810

(16) Van Norman, G. A. Limitations of Animal Studies for Predicting Toxicity in Clinical Trials: Is it Time to Rethink Our Current Approach? *JACC Basic Transl Sci* **2019**, *4* (7), 845-854. DOI: 10.1016/j.jacbts.2019.10.008
(17) Peaston, A. E.; Whitelaw, E. Epigenetics and phenotypic variation in mammals. *Mamm Genome* **2006**, *17* (5), 365-374. DOI: 10.1007/s00335-005-0180-2
(18) Ning, M.; Duarte, J. D.; Stevison, F.; Isoherranen, N.; Rubin, L. H.; Jeong, H. Determinants of Cytochrome P450 2D6 mRNA Levels in Healthy Human Liver Tissue. *Clin Transl Sci* **2019**, *12* (4), 416-423. DOI: 10.1111/cts.12632
(19) Ning, M.; Duarte, J. D.; Rubin, L. H.; Jeong, H. CYP2D6 Protein Level Is the Major Contributor to Interindividual Variability in CYP2D6-Mediated Drug Metabolism in Healthy Human Liver Tissue. *Clin Pharmacol Ther* **2018**, *104* (5), 974-982. DOI: 10.1002/cpt.1032
(20) Gerardo-Nava, J. L.; Jansen, J.; Gunther, D.; Klasen, L.; Thiebes, A. L.; Niessing, B.; Bergerbit, C.; Meyer, A. A.; Linkhorst, J.; Barth, M.; et al. Transformative Materials to Create 3D Functional Human Tissue Models In Vitro in a Reproducible Manner. *Adv Healthc Mater* **2023**, *12* (20), e2301030. DOI: 10.1002/adhm.202301030
(21) Leung, C. M.; de Haan, P.; Ronaldson-Bouchard, K.; Kim, G.-A.; Ko, J.; Rho, H. S.; Chen, Z.; Habibovic, P.; Jeon, N. L.; Takayama, S.; et al. A guide to the organ-on-a-chip. *Nature Reviews Methods Primers* **2022**, *2* (1). DOI: 10.1038/s43586-022-00118-6
(22) Low, L. A.; Mummery, C.; Berridge, B. R.; Austin, C. P.; Tagle, D. A. Organs-on-chips: into the next decade. *Nat Rev Drug Discov* **2021**, *20* (5), 345-361. DOI: 10.1038/s41573-020-0079-3
(23) Sackett, S. D.; Tremmel, D. M.; Ma, F.; Feeney, A. K.; Maguire, R. M.; Brown, M. E.; Zhou, Y.; Li, X.; O'Brien, C.; Li, L.; et al. Extracellular matrix scaffold and hydrogel derived from decellularized and delipidized human pancreas. *Sci Rep* **2018**, *8* (1), 10452. DOI: 10.1038/s41598-018-28857-1
(24) Kolesky, D. B.; Homan, K. A.; Skylar-Scott, M. A.; Lewis, J. A. Three-dimensional bioprinting of thick vascularized tissues. *Proceedings of the National Academy of Sciences* **2016**, *113* (12), 3179-3184. DOI: 10.1073/pnas.1521342113 (acccessed 2022-03-06 00:16:49).
(25) Beller, N. C.; Wang, Y.; Hummon, A. B. Evaluating the Pharmacokinetics and Pharmacodynamics of Chemotherapeutics within a Spatial SILAC-Labeled Spheroid Model System. *Anal Chem* **2023**, *95* (30), 11263-11272. DOI: 10.1021/acs.analchem.3c00905
(26) Shannon, A. E.; Boos, C. E.; Hummon, A. B. Co-culturing multicellular tumor models: Modeling the tumor microenvironment and analysis techniques. *Proteomics* **2021**, *21* (9), e2000103. DOI: 10.1002/pmic.202000103
(27) Malik, M.; Yang, Y.; Fathi, P.; Mahler, G. J.; Esch, M. B. Critical Considerations for the Design of Multi-Organ Microphysiological Systems (MPS). *Frontiers in Cell and Developmental Biology* **2021**, *9*, 721338. DOI: 10.3389/fcell.2021.721338 (acccessed 2023-07-04 16:49:15).
(28) Lee, H.; Yang, X.; Jin, P. R.; Won, K. J.; Kim, C. H.; Jeong, H. The Discovery of Gut Microbial Metabolites as Modulators of Host Susceptibility to Acetaminophen-Induced Hepatotoxicity. *Drug Metab Dispos* **2024**, *52* (8), 754-764. DOI: 10.1124/dmd.123.001541
(29) Lin, J.; Sahakian, D. C.; de Morais, S. M.; Xu, J. J.; Polzer, R. J.; Winter, S. M. The role of absorption, distribution, metabolism, excretion and toxicity in drug discovery. *Curr Top Med Chem* **2003**, *3* (10), 1125-1154. DOI: 10.2174/1568026033452096
(30) Serras, A. S.; Rodrigues, J. S.; Cipriano, M.; Rodrigues, A. V.; Oliveira, N. G.; Miranda, J. P. A Critical Perspective on 3D Liver Models for Drug Metabolism and Toxicology Studies. *Front Cell Dev Biol* **2021**, *9*, 626805. DOI: 10.3389/fcell.2021.626805

(31) Hruban, Z. Pulmonary and generalized lysosomal storage induced by amphiphilic drugs. *Environ Health Perspect* **1984**, *55*, 53-76. DOI: 10.1289/ehp.845553
(32) Rautio, J.; Meanwell, N. A.; Di, L.; Hageman, M. J. The expanding role of prodrugs in contemporary drug design and development. *Nat Rev Drug Discov* **2018**, *17* (8), 559-587. DOI: 10.1038/nrd.2018.46
(33) Najjar, A.; Karaman, R. The prodrug approach in the era of drug design. *Expert Opin Drug Deliv* **2019**, *16* (1), 1-5. DOI: 10.1080/17425247.2019.1553954
(34) Pond, S. M.; Tozer, T. N. First-Pass Elimination Basic Concepts and Clinical Consequences. *Clinical Pharmacokinetics* **1984**, *9* (1), 1-25. DOI: 10.2165/00003088-198409010-00001
(35) Lynch, T.; Price, A. The effect of cytochrome P450 metabolism on drug response, interactions, and adverse effects. *Am Fam Physician* **2007**, *76* (3), 391-396.
(36) Ewart, L.; Apostolou, A.; Briggs, S. A.; Carman, C. V.; Chaff, J. T.; Heng, A. R.; Jadalannagari, S.; Janardhanan, J.; Jang, K. J.; Joshipura, S. R.; et al. Performance assessment and economic analysis of a human Liver-Chip for predictive toxicology. *Commun Med (Lond)* **2022**, *2* (1), 154. DOI: 10.1038/s43856-022-00209-1
(37) Jang, K. J.; Otieno, M. A.; Ronxhi, J.; Lim, H. K.; Ewart, L.; Kodella, K. R.; Petropolis, D. B.; Kulkarni, G.; Rubins, J. E.; Conegliano, D.; et al. Reproducing human and cross-species drug toxicities using a Liver-Chip. *Sci Transl Med* **2019**, *11* (517). DOI: 10.1126/scitranslmed.aax5516
(38) Rajan, S. A. P.; Sherfey, J.; Ohri, S.; Nichols, L.; Smith, J. T.; Parekh, P.; Kadar, E. P.; Clark, F.; George, B. T.; Gregory, L.; et al. A Novel Milli-fluidic Liver Tissue Chip with Continuous Recirculation for Predictive Pharmacokinetics Applications. *AAPS J* **2023**, *25* (6), 102. DOI: 10.1208/s12248-023-00870-x
(39) McKee, C.; Chaudhry, G. R. Advances and challenges in stem cell culture. *Colloids Surf B Biointerfaces* **2017**, *159*, 62-77. DOI: 10.1016/j.colsurfb.2017.07.051
(40) Kvist, A. J.; Kanebratt, K. P.; Walentinsson, A.; Palmgren, H.; O'Hara, M.; Bjorkbom, A.; Andersson, L. C.; Ahlqvist, M.; Andersson, T. B. Critical differences in drug metabolic properties of human hepatic cellular models, including primary human hepatocytes, stem cell derived hepatocytes, and hepatoma cell lines. *Biochem Pharmacol* **2018**, *155*, 124-140. DOI: 10.1016/j.bcp.2018.06.026
(41) Stanley, L. A.; Wolf, C. R. Through a glass, darkly? HepaRG and HepG2 cells as models of human phase I drug metabolism. *Drug Metab Rev* **2022**, *54* (1), 46-62. DOI: 10.1080/03602532.2022.2039688
(42) Kanebratt, K. P.; Andersson, T. B. Evaluation of HepaRG cells as an in vitro model for human drug metabolism studies. *Drug Metab Dispos* **2008**, *36* (7), 1444-1452. DOI: 10.1124/dmd.107.020016
(43) Guillouzo, A.; Corlu, A.; Aninat, C.; Glaise, D.; Morel, F.; Guguen-Guillouzo, C. The human hepatoma HepaRG cells: a highly differentiated model for studies of liver metabolism and toxicity of xenobiotics. *Chem Biol Interact* **2007**, *168* (1), 66-73. DOI: 10.1016/j.cbi.2006.12.003
(44) Jackson, J. P.; Li, L.; Chamberlain, E. D.; Wang, H.; Ferguson, S. S. Contextualizing Hepatocyte Functionality of Cryopreserved HepaRG Cell Cultures. *Drug Metab Dispos* **2016**, *44* (9), 1463-1479. DOI: 10.1124/dmd.116.069831
(45) Hotaling, N. A.; Bharti, K.; Kriel, H.; Simon, C. G., Jr. DiameterJ: A validated open source nanofiber diameter measurement tool. *Biomaterials* **2015**, *61*, 327-338. DOI: 10.1016/j.biomaterials.2015.05.015

(46) Moore, P. A.; Hersh, E. V.; Papas, A. S.; Goodson, J. M.; Yagiela, J. A.; Rutherford, B.; Rogy, S.; Navalta, L. Pharmacokinetics of Lidocaine With Epinephrine Following Local Anesthesia Reversal With Phentolamine Mesylate. *Anesthesia Progress* **2008**, *55* (2), 40-48. DOI: 10.2344/0003-3006(2008)55[40:Polwef]2.0.Co;2
(47) Jin, Y.; He, C.; Di, X.; Fu, L.; Qi, X.; Liu, R.; Zheng, L.; Wang, Y.; Wang, Z.; Tu, F. Simultaneous determination of lidocaine and its active metabolites in plasma by UPLC-MS/MS and application to a clinical pharmacokinetic study in liver cancer patients with laparoscopic hepatectomy. *J Chromatogr B Analyt Technol Biomed Life Sci* **2022**, *1207*, 123362. DOI: 10.1016/j.jchromb.2022.123362
(48) Ramon, Y.; Barak, Y.; Ullmann, Y.; Hoffer, E.; Yarhi, D.; Bentur, Y. Pharmacokinetics of high-dose diluted lidocaine in local anesthesia for facelift procedures. *Ther Drug Monit* **2007**, *29* (5), 644-647. DOI: 10.1097/FTD.0b013e3180eaa10a
(49) Martell, B.; Kushner, H.; Richardson, E.; Mize, A.; Mayer, P. Pharmacokinetics of Lidocaine and Its Metabolites Following Vaginal Administration of Lidocaine Gel to Healthy Female Subjects. *Clin Pharmacol Drug Dev* **2017**, *6* (1), 27-35. DOI: 10.1002/cpdd.286
(50) Huang, W.; Isoherranen, N. Sampling Site Has a Critical Impact on Physiologically Based Pharmacokinetic Modeling. *J Pharmacol Exp Ther* **2020**, *372* (1), 30-45. DOI: 10.1124/jpet.119.262154
(51) Rao Yadlapalli, S. S.; Katari, N. K.; Manabolu Surya, S. B.; Karra, V. K.; Kommineni, V.; Jonnalagadda, S. B. Simultaneous quantification of lidocaine and prilocaine in human plasma by LC-MS/MS and its application in a human pharmacokinetic study. *Pract Lab Med* **2019**, *17*, e00129. DOI: 10.1016/j.plabm.2019.e00129
(52) Gudin, J.; Argoff, C.; Fudin, J.; Greuber, E.; Vought, K.; Patel, K.; Nalamachu, S. A Randomized, Open-Label, Bioequivalence Study of Lidocaine Topical System 1.8% and Lidocaine Patch 5% in Healthy Subjects. *J Pain Res* **2020**, *13*, 1485-1496. DOI: 10.2147/JPR.S237934
(53) Disanto, A. R.; Golden, G. Effect of food on the pharmacokinetics of clozapine orally disintegrating tablet 12.5 mg: a randomized, open-label, crossover study in healthy male subjects. *Clin Drug Investig* **2009**, *29* (8), 539-549. DOI: 10.2165/00044011-200929080-00004
(54) Abdallah, M. H.; Shahien, M. M.; El-Horany, H. E.; Ahmed, E. H.; El-Nahas, H. M.; Abdulla, N. A.; Ibrahim, T. M. Evaluation of Mucoadhesive Nano-Bilosomal In Situ Gels Containing Anti-Psychotic Clozapine for Treatment of Schizophrenia: In Vitro and In Vivo Studies. *Pharmaceuticals (Basel)* **2024**, *17* (10). DOI: 10.3390/ph17101404
(55) Tassaneeyakul, W.; Kittiwattanagul, K.; Vannaprasaht, S.; Kampan, J.; Tawalee, A.; Puapairoj, P.; Tiamkao, S.; Juthagridsada, S.; Kukongviriyapan, V.; Tassaneeyakul, W. Steady-state bioequivalence study of clozapine tablet in schizophrenic patients. *J Pharm Pharm Sci* **2005**, *8* (1), 47-53.
(56) Glue, P.; Gale, C.; Menkes, D. B.; Hung, N. Evaluation of bioequivalence between clozapine suspension and tablet formulations : a multiple-dose, fed and fasted study. *Clin Drug Investig* **2012**, *32* (11), 723-727. DOI: 10.1007/s40261-012-0004-6
(57) Golden, G.; Honigfeld, G. Bioequivalence of clozapine orally disintegrating 100-mg tablets compared with clozapine solid oral 100-mg tablets after multiple doses in patients with schizophrenia. *Clin Drug Investig* **2008**, *28* (4), 231-239. DOI: 10.2165/00044011-200828040-00004

(58) Lee, J.; Kim, M. G.; Jeong, H. C.; Shin, K. H. Physiologically-based pharmacokinetic model for clozapine in Korean patients with schizophrenia. *Transl Clin Pharmacol* **2021**, *29* (1), 33-44. DOI: 10.12793/tcp.2021.29.e3
(59) Wongsinsup, C. Determination of Clozapine in Human Plasma by High – Performance Liquid Chromatography with UV – VIS Detector. *Chiang Mai University Journal of Natural Sciences* **2010**, *9* (1).
(60) Bennett, P. N.; Aarons, L. J.; Bending, M. R.; Steiner, J. A.; Rowland, M. Pharmacokinetics of lidocaine and its deethylated metabolite: dose and time dependency studies in man. *J Pharmacokinet Biopharm* **1982**, *10* (3), 265-281. DOI: 10.1007/BF01059261
(61) Thomson, A. H.; Elliott, H. L.; Kelman, A. W.; Meredith, P. A.; Whiting, B. The pharmacokinetics and pharmacodynamics of lignocaine and MEGX in healthy subjects. *J Pharmacokinet Biopharm* **1987**, *15* (2), 101-115. DOI: 10.1007/BF01062338
(62) Foong, K. W.; Chaw, S. H.; Lo, Y. L.; Loh, P. S. Population Pharmacokinetics of Intravenous Lidocaine in Adults: A Systematic Review. *Clin Pharmacokinet* **2024**, *63* (5), 623-643. DOI: 10.1007/s40262-024-01373-4
(63) Jann, M. W. Clozapine. *Pharmacotherapy: The Journal of Human Pharmacology and Drug Therapy* **2012**, *11* (3), 179-195. DOI: 10.1002/j.1875-9114.1991.tb02628.x
(64) Albitar, O.; Harun, S. N.; Zainal, H.; Ibrahim, B.; Sheikh Ghadzi, S. M. Population Pharmacokinetics of Clozapine: A Systematic Review. *Biomed Res Int* **2020**, *2020*, 9872936. DOI: 10.1155/2020/9872936
(65) Poulin, P.; Kenny, J. R.; Hop, C. E.; Haddad, S. In vitro-in vivo extrapolation of clearance: modeling hepatic metabolic clearance of highly bound drugs and comparative assessment with existing calculation methods. *J Pharm Sci* **2012**, *101* (2), 838-851. DOI: 10.1002/jps.22792
(66) Jann, M. W.; Grimsley, S. R.; Gray, E. C.; Chang, W.-H. Pharmacokinetics and Pharmacodynamics of Clozapine. *Clinical Pharmacokinetics* **1993**, *24* (2), 161-176. DOI: 10.2165/00003088-199324020-00005
(67) Wilson, Z. E.; Rostami-Hodjegan, A.; Burn, J. L.; Tooley, A.; Boyle, J.; Ellis, S. W.; Tucker, G. T. Inter-individual variability in levels of human microsomal protein and hepatocellularity per gram of liver. *Br J Clin Pharmacol* **2003**, *56* (4), 433-440. DOI: 10.1046/j.1365-2125.2003.01881.x
(68) Molina, D. K.; DiMaio, V. J. M. Normal Organ Weights in Men: Part II—The Brain, Lungs, Liver, Spleen, and Kidneys. *The American Journal of Forensic Medicine and Pathology* **2012**, *33* (4), 368-372. DOI: 10.1097/PAF.0b013e31823d29ad
(69) Hedaya, M. A. *Basic pharmacokinetics*; Routledge, 2023.
(70) Baiocchini, A.; Montaldo, C.; Conigliaro, A.; Grimaldi, A.; Correani, V.; Mura, F.; Ciccosanti, F.; Rotiroti, N.; Brenna, A.; Montalbano, M.; et al. Extracellular Matrix Molecular Remodeling in Human Liver Fibrosis Evolution. *PLoS One* **2016**, *11* (3), e0151736. DOI: 10.1371/journal.pone.0151736
(71) Mazza, G.; Rombouts, K.; Rennie Hall, A.; Urbani, L.; Vinh Luong, T.; Al-Akkad, W.; Longato, L.; Brown, D.; Maghsoudlou, P.; Dhillon, A. P.; et al. Decellularized human liver as a natural 3D-scaffold for liver bioengineering and transplantation. *Sci Rep* **2015**, *5*, 13079. DOI: 10.1038/srep13079
(72) Gupta, S.; Sharma, A.; Rajakannu, M.; Bisevac, J.; Rela, M.; Verma, R. S. Small Molecule-Mediated Stage-Specific Reprogramming of MSCs to Hepatocyte-Like Cells and Hepatic Tissue for Liver Injury Treatment. *Stem Cell Rev Rep* **2024**, *20* (8), 2215-2235. DOI: 10.1007/s12015-024-10771-x

(73) Xue, J.; Wu, T.; Dai, Y.; Xia, Y. Electrospinning and Electrospun Nanofibers: Methods, Materials, and Applications. *Chem Rev* **2019**, *119* (8), 5298-5415. DOI: 10.1021/acs.chemrev.8b00593
(74) Feltz, K. P.; Growney Kalaf, E. A.; Chen, C.; Martin, R. S.; Sell, S. A. A review of electrospinning manipulation techniques to direct fiber deposition and maximize pore size. *Electrospinning* **2017**, *2* (1), 46-61. DOI: 10.1515/esp-2017-0002 (acccessed 2023-06-17 17:17:48).
(75) Terrell, J. A.; Jones, C. G.; Kabandana, G. K. M.; Chen, C. From cells-on-a-chip to organs-on-a-chip: scaffolding materials for 3D cell culture in microfluidics. *Journal of Materials Chemistry B* **2020**, *8* (31), 6667-6685. DOI: 10.1039/D0TB00718H (acccessed 2023-06-17 17:17:05).
(76) Chen, C.; Townsend, A. D.; Hayter, E. A.; Birk, H. M.; Sell, S. A.; Martin, R. S. Insert-based microfluidics for 3D cell culture with analysis. *Analytical and Bioanalytical Chemistry* **2018**, *410* (12), 3025-3035. DOI: 10.1007/s00216-018-0985-y (acccessed 2023-06-17 17:19:01).
(77) Ntonas, A.; Katsourakis, A.; Galanis, N.; Filo, E.; Noussios, G. Comparative Anatomical Study Between the Human and Swine Liver and Its Importance in Xenotransplantation. *Cureus* **2020**, *12* (7), e9411. DOI: 10.7759/cureus.9411
(78) Lada, E.; Anna, M.; Patrik, M.; Zbynek, T.; Miroslav, J.; Hynek, M.; Richard, P.; Sarah, L.; Vaclav, L. Porcine Liver Anatomy Applied to Biomedicine. *J Surg Res* **2020**, *250*, 70-79. DOI: 10.1016/j.jss.2019.12.038
(79) Junqueira, L. C.; Bignolas, G.; Brentani, R. R. Picrosirius staining plus polarization microscopy, a specific method for collagen detection in tissue sections. *Histochem J* **1979**, *11* (4), 447-455. DOI: 10.1007/BF01002772
(80) Wegner, K. A.; Keikhosravi, A.; Eliceiri, K. W.; Vezina, C. M. Fluorescence of Picrosirius Red Multiplexed With Immunohistochemistry for the Quantitative Assessment of Collagen in Tissue Sections. *J Histochem Cytochem* **2017**, *65* (8), 479-490. DOI: 10.1369/0022155417718541
(81) de Hoyos-Vega, J. M.; Hong, H. J.; Stybayeva, G.; Revzin, A. Hepatocyte cultures: From collagen gel sandwiches to microfluidic devices with integrated biosensors. *APL Bioeng* **2021**, *5* (4), 041504. DOI: 10.1063/5.0058798
(82) Bill, T. J.; Clayman, M. A.; Morgan, R. F.; Gampper, T. J. Lidocaine metabolism pathophysiology, drug interactions, and surgical implications. *Aesthet Surg J* **2004**, *24* (4), 307-311. DOI: 10.1016/j.asj.2004.05.001
(83) Torp KD, M. E., Simon LV. *Lidocaine Toxicity*. StatPearls Publishing, 2022. www.ncbi.nlm.nih.gov/books/NBK482479/ (accessed 12/11/2024).
(84) Marinho, E. Clozapine: A special case of an atypical antipsychotic. *European Journal of Medicinal Chemistry Reports* **2024**, *10*. DOI: 10.1016/j.ejmcr.2024.100140
(85) Perez-Caballero, L.; Torres-Sanchez, S.; Bravo, L.; Mico, J. A.; Berrocoso, E. Fluoxetine: a case history of its discovery and preclinical development. *Expert Opin Drug Discov* **2014**, *9* (5), 567-578. DOI: 10.1517/17460441.2014.907790
(86) Deodhar, M.; Rihani, S. B. A.; Darakjian, L.; Turgeon, J.; Michaud, V. Assessing the Mechanism of Fluoxetine-Mediated CYP2D6 Inhibition. *Pharmaceutics* **2021**, *13* (2). DOI: 10.3390/pharmaceutics13020148